Supporting Information for:
"Evidence for multiple Ferrel-like cells on Jupiter"

Keren Duer[1*], Nimrod Gavriel[1*], Eli Galanti[1], Yohai Kaspi[1],
Leigh N. Fletcher[2], Tristan Guillot[3], Scott J. Bolton[4], Steven M. Levin[5],
Sushil K. Atreya[6], Davide Grassi[7], Andrew P. Ingersoll[8], Cheng Li[6], Liming Li[9],
Jonathan I. Lunine[10], Glenn S. Orton[5], Fabiano A. Oyafuso[5], J. Hunter Waite, Jr.[4]

September 28, 2021

[1] *Department of Earth and Planetary Sciences, Weizmann Institute of Science, Rehovot, Israel*
[2] *School of Physics and Astronomy, University of Leicester, University Road, Leicester, LE1 7RH, UK*
[3] *Universitié Côte d'Azur, OCA, Lagrange CNRS, 06304 Nice, France*
[4] *Southwest Research Institute, San Antonio, Texas, TX, USA*
[5] *Jet Propulsion Laboratory, California Institute of Technology, 4800 Oak Grove Drive, Pasadena, CA 91109, USA*
[6] *Department of Climate and Space Sciences and Engineering, University of Michigan, Ann Arbor, MI, USA*
[7] *Istituto di Astrofisica e Planetologia Spaziali, INAF, Rome, Italy*
[8] *California Institute of Technology, Pasadena, California, USA*
[9] *University of Houston, Houston, TX, USA*
[10] *Department of Astronomy, Cornell University, Ithaca, New York 14853, USA*

* These authors contributed equally to this work

S1 Eddy momentum driven Ferrel-like cell

S1.1 Standard formulation

Using approximations similar to the commonly used formulation which describe the terrestrial Ferrel-cell dynamics [*Vallis*, 2017], the leading order zonal mean zonal momentum equation may be written as

$$\frac{\partial \bar{u}}{\partial t} + \frac{\partial}{\partial y}\left(\overline{u'v'}\right) - f\bar{v} = -F_{\text{sink}}, \tag{S1}$$

where F_{sink} is a sink term. On Earth, the sink term represents a surface drag in the Ekman layer and in the Jovian atmosphere, if the cells are as deep as the jets [*Kaspi et al.*, 2020], it might be Ohmic dissipation [*Liu et al.*, 2008; *Liu and Schneider*, 2010; *Kaspi et al.*, 2020] (i.e., $F_{\text{sink}} = \frac{1}{4\pi\bar{\rho}}\overline{(\nabla \times \mathbf{B}) \times \mathbf{B}}$, where $\mathbf{B}$ is the 3D magnetic field and ρ is density). Eq. 1[1], adequate for the upper branch of the cells, results from applying time-averaging away from the sink layer. This balance leads to meridional velocities in the directions illustrated in Fig. 2b[2]. Alternatively,

[1]Note that equation cross-references without a S refer to equations in the main text.
[2]Note that figure cross-references without a S refer to figures in the main text.

applying vertical integration cancels the Coriolis terms in the vertical boundaries of the cell and the relation between the zonal jets, their eddy source term and the sink term becomes

$$\frac{\partial \bar{U}}{\partial t} = -\frac{\partial}{\partial y}\left(\overline{U'V'}\right) - \hat{F}_{\text{sink}}. \tag{S2}$$

where U and V are the vertically integrated velocities, and $\hat{F}_{\text{sink}}$ is the vertically integrated sink term. Therefore, converging (diverging) eddy momentum fluxes transfer their momentum to eastward (westward) jets, as can be seen in the Jovian atmosphere (Fig. 1b,d). In the descriptions throughout this study, Cartesian approximations are used for the sake of clarity, but the actual calculations were performed using the spherical, more accurate, formulations.

S1.2 TEM formulation for Jupiter

The Transformed Eulerian Mean (TEM) equations, commonly invoked to quantify Lagrangian mass-transport in Earth's Ferrel cells, describe a circulation driven by the diabatic heating term [*Vallis*, 2017]. The TEM formulation can be derived from the momentum and thermodynamic equations, under Boussinesq and quasi-geostrophic approximations (*Vallis* [2017], ch. 10.3), resulting in

$$\frac{\partial \bar{u}}{\partial t} - f\bar{v}^{*} = \nabla \cdot \boldsymbol{F}, \tag{S3}$$

and

$$\frac{\partial \bar{b}}{\partial t} - \bar{w}^{*} N^2 = \bar{S}, \tag{S4}$$

where $\bar{v}^{*} = \bar{v} - \frac{\partial}{\partial z}\left(\frac{1}{N^2}\overline{v'b'}\right)$ and $\bar{w}^{*} = \bar{w} + \frac{\partial}{\partial y}\left(\frac{1}{N^2}\overline{v'b'}\right)$ are defined as the "residual" mean meridional and vertical velocities, respectively, which approximate mass-transport by both Eulerian mean velocities and eddy fluxes, $N^2 = {}^{\partial \bar{b}_0}/_{\partial z}$ is the Brunt–Väisälä frequency, $\bar{S}$ is the diabatic heating term, and $\boldsymbol{F} = -\left(u'v'\right)\hat{\mathbf{j}} + \left(\frac{f}{N^2}\overline{v'b'}\right)\hat{\boldsymbol{k}}$ is the Elissan-Plam (EP) flux. b_0 and b represent the mean (zonally- and meridionally-averaged) and the deviation from the mean of the buoyancy force and $\hat{\mathbf{j}}$ ($\hat{\mathbf{k}}$) is a unit vectors in the meridional (vertical) direction. On Earth, the diabatic heating term is important [*Lachmy and Kaspi*, 2020], and therefore the residual meridional velocities accurately represent the total meridional transport of mass in Earth's midlatitudes.

The midlatitude atmosphere on Earth is characterized by baroclinicity, and as a result, the second term of the EP flux is substantial and plays a key role in the resulting circulation. On Jupiter, the eddy fluxes beneath the cloud level and the diabatic heating are yet to be measured. However, gravity-measurement analysis implies that Jupiter's jets are nearly barotropic in the depth range relevant to this study [*Galanti and Kaspi*, 2021], meaning that the EP flux is dominated by the first term, and $\bar{w}^{*}$ is comparable to $\bar{w}$ [*Lee and Kaspi*, 2021]. Therefore, under the barotropic limit, the equations describing the Eulerian velocities in a Ferrel-like cell might also represent the total mass transport in the Jovian cells.

S1.3 Correlation analysis

The picture illustrated in Fig. 2, relating the distribution of ammonia and the zonal winds according to the Ferrel-like cells hypothesis, is tested quantitatively in a correlation analysis exhibited in Fig. 3. The expected relations between the zonal jets and the ammonia meridional gradients in the NH are

$$\bar{u} \propto \begin{cases} -\partial_y m_a & 1.5 \leq p < 6\,\text{bar} \quad (\text{channels } 4-5)\,, \\ \partial_y m_a & p \geq 6\,\text{bar} \quad (\text{channels } 1-3)\,,\ p < 1.5\,\text{bar} \quad (\text{channel } 6)\,. \end{cases} \tag{S5}$$

Here, $\partial_y m_a$ is the latitudinal gradient of the ammonia concentration (m_a) and p is pressure. The channels refer to the six frequencies of Juno's MWR. In the SH, as the circulation is reversed, Eq. S5 flips signs. Eq. S5 captures also the case of cells with westward jets, as both $\bar{u}$ and $\partial_y m_a$ change sign. A Pearson correlation coefficient ($\mathscr{S}(\vartheta, \mathrm{ch})$) is calculated for each latitude and MWR channel, and its value is represented by a color between blue, representing a negative correlation, white, representing no correlation and red, representing a positive correlation. The T_b data is measured in a resolution of $\sim 0.6^\circ$ latitude. The data is interpolated such that the grid size is 0.1° latitude, and the correlation for each point ϑ_i is calculated along a span $\{\vartheta_i - 2^\circ, \vartheta_i + 2^\circ\}$. This choice of a 4° latitudinal bin allows having enough data points for the statistical value of the correlation (more than 6 data pairs), and ensures the local nature of the results. The correlations on the MWR data are calculated between the following trends. In Fig. 3a, channels 1-3 and 6 and in Fig. 3c channels 4-5 the color represents the correlation $\bar{u} \propto \partial_y T_\mathrm{b}$. In Fig. 3a, channels 4-5 and in Fig. 3c channels 1-3 and 6 the color represents the correlation $\bar{u} \propto -\partial_y T_\mathrm{b}$. Note that anomalies of brightness temperature and ammonia abundance are inversely proportional [*Li et al.*, 2017]. In Fig. 3b the correlations at all channels are calculated according to $\bar{u} \propto -T_\mathrm{b}$. Here, T_b is the Nadir component of the brightness temperate [°K] (other emission angles were not included in the analysis), averaged over nine Juno orbits (PJs $1, 3, 4, 5, 6, 7, 8, 9$ and 12) [*Oyafuso et al.*, 2020]. For further discussion regarding limb-darkening T_b we point the readers to *Fletcher et al.* [2021]. $\bar{u}$ is Jupiter's zonally-averaged zonal wind [m s^{-1}] measured by the Hubble space telescope during Juno's third perijove [*Tollefson et al.*, 2017], projected barotropically along the axis of rotation [*Galanti and Kaspi*, 2021; *Galanti et al.*, 2021]. The ammonia distribution by JIRAM is estimated at a depth of ~ 6 bar, which is the depth where a local minimum appears in M_a (Fig. 2a). Arbitrarily, the correlation is performed according to $p > 6$ bar in Eq. 2 (Fig. 2d) and the overall positive result points that indeed the depth level of JIRAM measurements should be deeper than the local minimum of M_a. The ammonia estimates from JIRAM are measured in a resolution of 1° latitude. Similar to the T_b correlation analysis, the data is interpolated, and the correlation is performed on a 4° latitude bin for consistency. In Fig. 3d (f) the color represents the correlation $\bar{u} \propto -\partial_y m_a$ ($\bar{u} \propto \partial_y m_a$) and in Fig. 3e the color represents the correlation $\bar{u} \propto m_a$. Finally, the eddy momentum flux convergence is measured in a resolution of 1° latitude, and the correlation is performed using the same latitudinal bin of 4°. In Fig. 3g (h) the color represents the correlation $\bar{u} \propto -\partial_y \left(\overline{u'v'}\right)$ ($\bar{u} \propto \partial_y \left(\overline{u'v'}\right)$).

We also examine the correlation between the zonal wind and the lightning gradient. We find a good match in the northern hemisphere and a weak negative correlation in the southern hemisphere, where Juno is much less sensitive to lightnings (Fig. S1). Note that the correlation between lightnings and the Ferrel cells is less indicative, as we should only examine the correlation in the rising branch of the cells. Therefore, the correlation values away from the rising branch should be regarded with caution.

S1.4 Advection-relaxation model

S1.4.1 T_b as an indicator for ammonia

As ammonia estimates by Juno's MWR for the high midlatitudes are not yet available, we express the T_b measurements as ammonia in order to examine the model results. For that, we define a reconstructed ammonia distribution from Juno MWR data ($m_a^{(\mathrm{data})}$), used as a benchmark for the advection-relaxation model, constructed by the mean ammonia calculated from MWR measurements of PJ1 (M_a, Fig. 2a) [*Li et al.*, 2017] and T_b measurements averaged over multiple Juno orbits (PJs 1-12) [*Oyafuso et al.*, 2020]. The standard deviation between the perijoves is computed as a function of latitude to validate that the latitudinal variations appearing in the T_b data are physical (Fig. S3 for the midlatitudes and Fig. S4 for the equatorial region). We estimate the T_b anomalies (T'_b) by removing the cross-channel average ($T_{\mathrm{b,mean}}(\mathrm{ch})$) from each MWR channel, and then decompose T'_b into Legendre polynomials and reconstruct the anomalies without the low polynomials to remove large scale variations. These variations, representing equator to pole radiation differences, are not related to ammonia variations by meridional

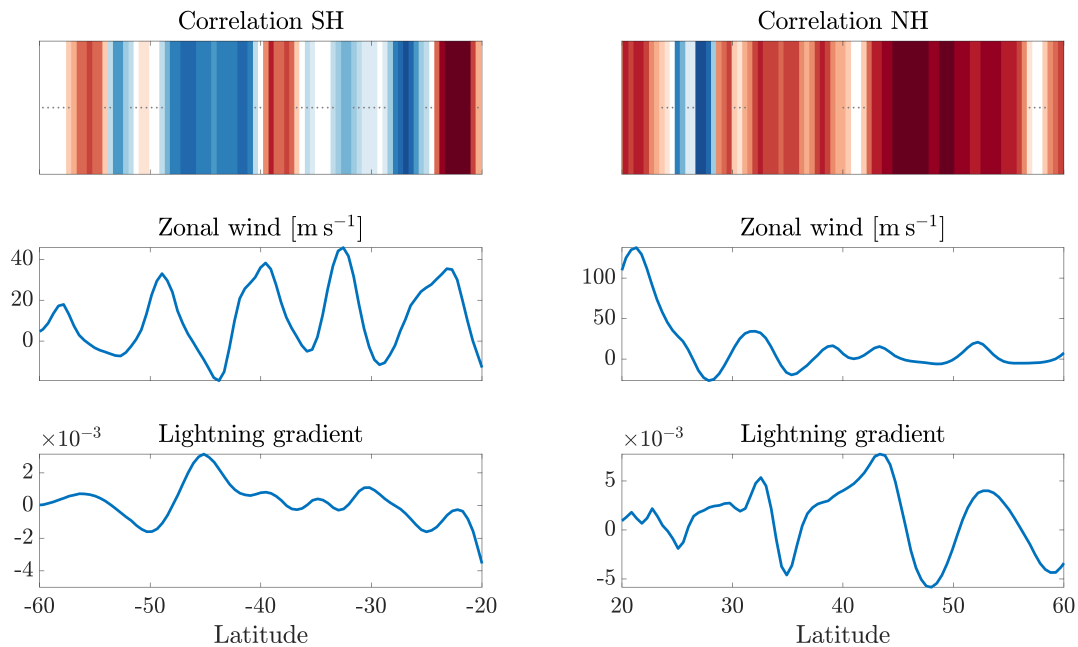

Figure S1: Correlation coefficients (upper panels) between the zonal wind (middle panels) and the lightning meridional gradient (lower panels) in the midlatitudes.

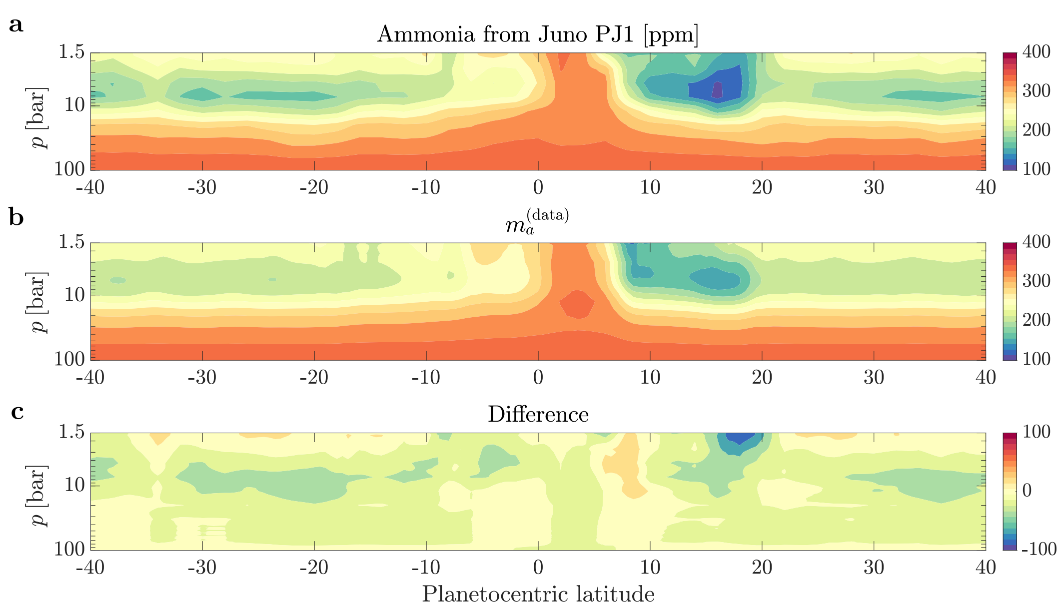

Figure S2: (a) Ammonia estimate [*Li et al.*, 2017] from Juno MWR PJ1 data. (b) m_a calculated from T_b (Eq. S8). This field is used as a benchmark ($m_a^{(\mathrm{data})}$) for the model results. (c) the difference between panel a and panel b.

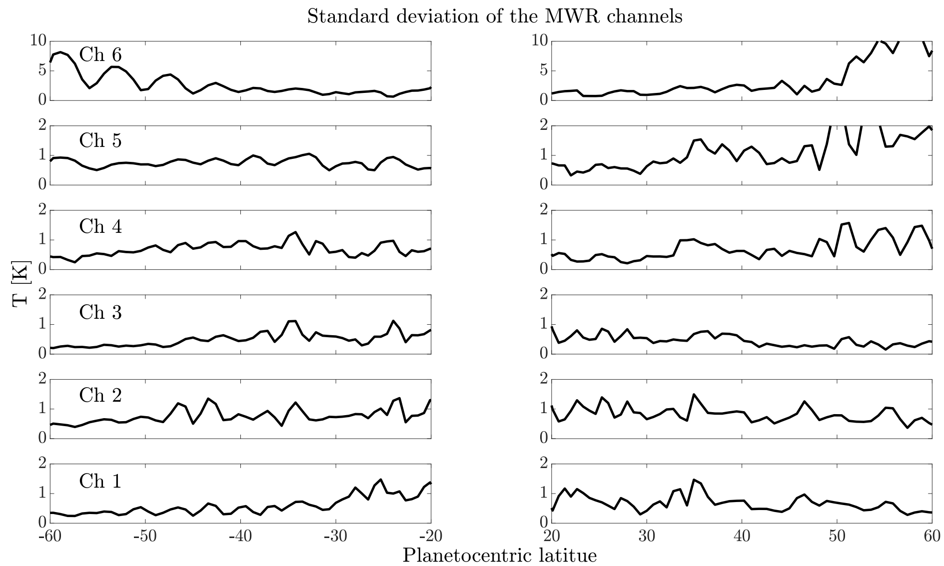

Figure S3: The standard deviation (STD) of the nadir T_b in the midlatitudes computed from nine different perijoves through PJs 1-12 [*Oyafuso et al.*, 2020], in the six MWR channels. The STD is computed after the trend removal for each perijove, as detailed in eq. S7. For channels 1-5, the STD values are smaller than the variation seen in the data (Fig. 1h). Note that although the STD values for channel 6 are higher, at some latitudes, than the mean latitudinal variation (of the same channel), this channel senses at altitudes which are above the cells identified in this study.

cells [*Oyafuso et al.*, 2020]. The reconstructed ammonia is then

$$T_\mathrm{b}'(\vartheta,\mathrm{ch}) = T_\mathrm{b}(\vartheta,\mathrm{ch}) - T_\mathrm{b,mean}(\mathrm{ch}) \cong \sum_{i=1}^{N} A_i(\vartheta,\mathrm{ch}) P_i\left(\sin\vartheta\right), \tag{S6}$$

$$T_\mathrm{b,rec}'(\vartheta,\mathrm{ch}) = \sum_{i=30}^{N} A_i(\vartheta,\mathrm{ch}) P_i\left(\sin\vartheta\right), \tag{S7}$$

$$m_a^{(\mathrm{data})}(\vartheta,\mathrm{ch}) = M_\mathrm{a}(\mathrm{ch}) - K(\mathrm{ch}) T_\mathrm{b,rec}'(\vartheta,\mathrm{ch}), \tag{S8}$$

where P_i are the Legendre polynomials, A_i are the associated coefficients, $N = 200$ is the number of polynomials used and K [ppm $\cdot$ degrees^{-1}] is a depth-dependent 'key', optimized at each depth using Matlab's `'fmincon'` to best fit the estimated ammonia distribution from PJ1 [*Li et al.*, 2017]. Note that T_b is available between latitudes 90°S to 90°N, therefore $P_{i=30}$ is equivalent to a wavelength of approximately 12° latitude. As the jets widths are not larger the 8° in latitude, this truncation removes variations that are not due to the existence of meridional Ferrel-like cells. The overall structure of $m_a^{(\mathrm{data})}$ is very similar to the ammonia map from PJ1 [*Li et al.*, 2017], while the meridional anomalies now represent well PJs 1-12 (Fig. S2). Finally, the resulting K ranges between 5 at 1 bar to 0 at depth and is used to estimate $m_a^{(\mathrm{data})}$ at latitudes 60°S to 60°N. The profile is interpolated between 1 and 240 bar, according to the relevant pressure levels of each channel (Fig. 4d). These levels are estimated according to the peak of the contribution function of each MWR channel, to give that channels $\{1, 2, 3, 4, 5, 6\}$ correspond to pressure levels of $\{240, 30, 9, 3, 1.5, 0.7\}$ bar [*Janssen et al.*, 2017; *Bolton et al.*, 2017].

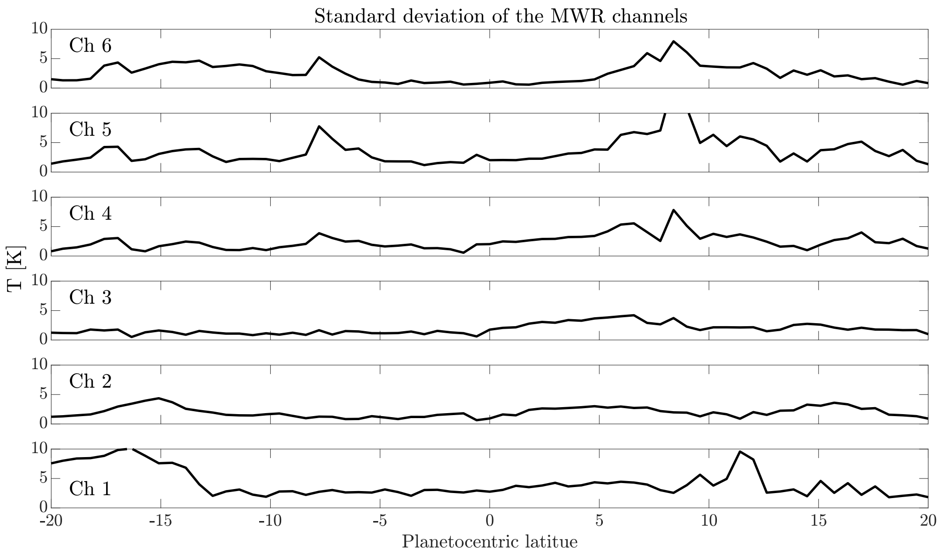

Figure S4: The equatorial standard deviation of the nadir $T_{\rm b}$ computed from nine different perijoves through PJs 1-12 [*Oyafuso et al.*, 2020], in the six MWR channels. The STD is computed on the original nadir coefficients.

S1.4.2 Cells construction and parameterization

To describe the meridional cells in the simplest manner, we parameterize each cell (indexed k) with an ellipse, according to a parameter l_k as follows

$$l_k = \sqrt{\frac{(d-a)^2}{a^2} + \frac{(\vartheta - \vartheta_k)^2}{b_k^2}}. \tag{S9}$$

Here, d is defined as downward distance from the cloud level, and a and b_k are the vertical and meridional extents of the cell, respectively. ϑ_k is the latitude of the center of cell k (black dots in Fig. S5a,b). b_k is set according to half the width of cell k (the distance between a black line and a black dot in Fig. S5a,b). The outline of cell k (representing the path of the peak tangential velocity along the cell) is thereby defined by $l_k = 1$. For simplicity, the velocities in a cell are defined using a normal distribution according to

$$\begin{aligned} v_k =& V_k \exp\left[-\frac{1}{2}\left(\frac{l_k - 1}{\widetilde{\sigma}}\right)^2\right] \sin\phi, \\ w_k =& V_k \exp\left[-\frac{1}{2}\left(\frac{l_k - 1}{\widetilde{\sigma}}\right)^2\right] \cos\phi, \\ \widetilde{\sigma} =& \sigma\left(\cos^2\vartheta + \frac{b_k}{a}\sin^2\vartheta\right), \end{aligned} \tag{S10}$$

where $\phi = \arctan\left[\frac{d-a}{R_{\rm J}\sin(\vartheta - \vartheta_k)}\right]$, $R_{\rm J}$ is Jupiter's radius and σ is a parameter for the broadness of a cell's branch. V_k represents the relative strength (velocity) of cell k, parameterized according to the square root of the averaged eddy momentum flux convergence within the cell (Fig. S5b), and its sign represents the cell's direction (clockwise/counter-clockwise), set according to the zonal wind sign at the center of the cell (Fig. S5a). The total wind is then

$$\bar{v}(r,\vartheta) = \sum_k v_k(r,\vartheta), \quad \bar{w}(r,\vartheta) = \sum_k w_k(r,\vartheta). \tag{S11}$$

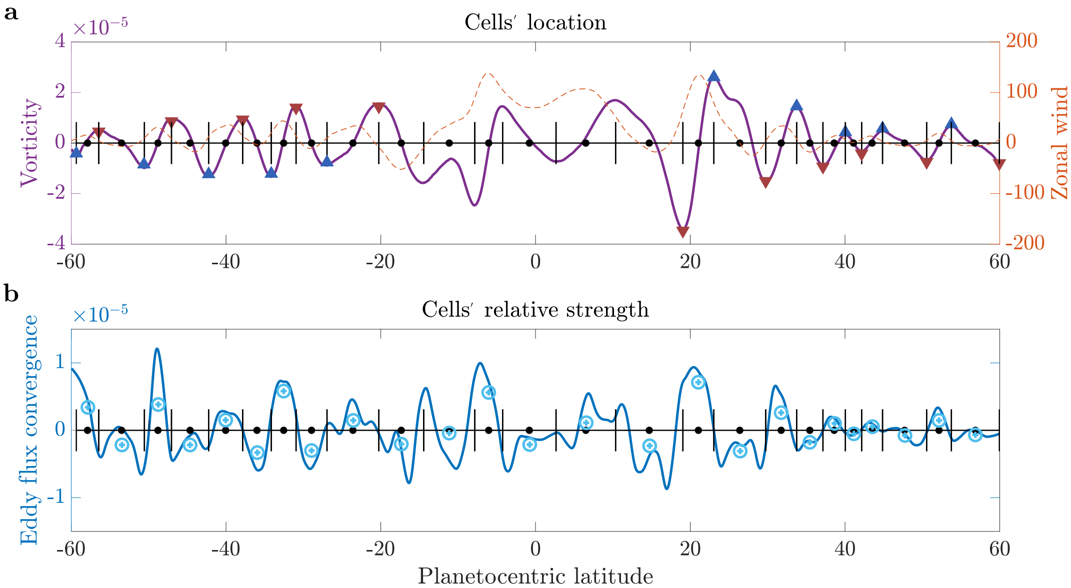

Figure S5: (a) Vorticity (purple) and zonal wind (dashed, orange). Blue (red) triangles represent vorticity peaks ($\partial\zeta/\partial y = 0$), where the vertical branches of the cells drive upward (downward) motion. The cells' centers are positioned between vorticity peaks (black dots), and the cells' extents ($2b_k$) are the distances between pairs of black lines. (b) Eddy momentum flux convergence (blue) and the cells' location as in panel a. Cells' relative strength is set by the averaged value of eddy flux convergence within the cell (light blue circles).

S1.4.3 Optimization and numerical solution

To solve for m_a, Eq. 3 is discretized using finite differences as

$$\bar{w}_{i,j}\frac{m_{i-1,j}-m_{i+1,j}}{2dr}+\bar{v}_{i,j}\frac{m_{i,j+1}-m_{i,j-1}}{2R_\mathrm{J}d\vartheta}=-G_i\left(m_{i,j}-M_i\right), \tag{S12}$$

where the "a" subscript of m and M was removed for clarity. Here i, and j are indices for the grid points in the r and ϑ directions, respectively. dr and $d\vartheta$ are the distances between adjacent points in each direction. Eq. S12 constitutes one of n^2 equations for n^2 variables, where n is the resolution of the grid in each direction. Eq. S12 is rearranged in a matrix form as $Ax = b$ such that m_a can be calculated from $A^{-1}b$.

The parameters G_i, σ and a are unknowns. For this, the Matlab optimization function `'fmincon'` is used for deciding G_i, σ and a to best reproduce the $m_a^{(\mathrm{data})}$ map. The cost function

$$f(G,\sigma,a)=\sum_{i,j}\left(\left|m_{i,j}^{(\mathrm{model})}-m_{i,j}^{(\mathrm{data})}\right|\right)^2 \tag{S13}$$

is the measure used to find the optimal parameters. The resulting value of G is shown in Fig. S6 for the case of G that is varying with depth, and for comparison, the solution with a constant G is shown as well. The value of σ was found to be ~ 0.85 in both cases. The parameter a was found to be ~ 1600 bar.

S1.4.4 Robustness analysis

To validate that the model results are robust and not sensitive to the specific parameters found by the optimization analysis, $m_{i,j}^{(\mathrm{model})}$ was also solved from equation 3 using a chosen set of parameters instead of the optimized set. The depth of the cells was chosen to be 3000 km ($a = 1500\,\mathrm{km}$), in accordance with the depth of the jets that was estimated from gravity measurements [*Kaspi et al.*, 2018]. The width of the cells was chosen such that one standard deviation covers half a cell's width ($\sigma = 0.5$). G is degenerated into a constant (no dependence in z) and

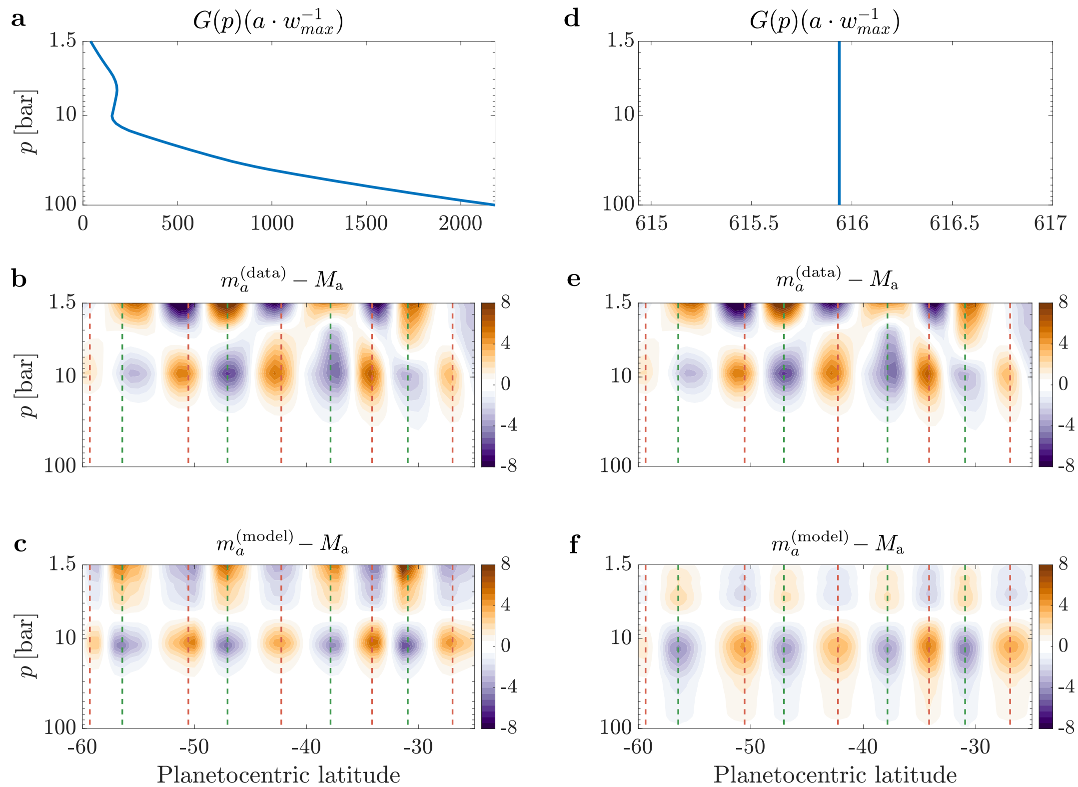

Figure S6: Comparison between model results with and without vertical variation in G. (a) The vertical variation of the normalized source term G used for Fig. 4c. b and e, $m_a^{(\mathrm{data})}$ anomalies [ppm] in the SH. (c) The ammonia anomalies [ppm] map produced by the advection-relaxation model with the source term from panel a. (d) Constant normalized source term G in Eq. 3. (f) The ammonia anomalies [ppm] map produced by the advection-relaxation model with the source tern from panel d. In panels b, c, e and f the vertical mean profile M_a is removed from the ammonia map m_a and dashed red and green lines are the upward and downward branches of the cells, respectively. The comparison reveals that although the solution with varying source term (a) results in a better model solution (**c**) compared to the measurements (b and d), the essence of the anomalies (f) is well captured with a constant source term (d).

is set, from a scaling argument, as $G = \max(w)/a\,[\mathrm{s}^{-1}]$. As seen in the results (Fig. S7), the modeled ammonia anomalies map still predicts the data convincingly. The main difference is the depth where the sign of the ammonia anomalies flip (between 3 and 6 bar), which is now only controlled by the input M_a [*Li et al.*, 2017], and could not be 'corrected' by a depth-dependent relaxation time scale. It can be seen that the essence of the circulation cells is still very apparent in the results.

S2 Equatorial region analysis

S2.1 Estimate for the extent of the equatorial region

The tangent cylinder is the projection (along the axis of rotation) of the planet's solid-body rotating core on the outer shell. The equatorial latitudes lie outside of the tangent cylinder, and is thereby characterized by a different dynamical regime than that of the midlatitudes. To separate quantitatively the midlatitudes, positioned within the tangent cylinder, from the equatorial region, it is required to know the depth of the atmosphere (D_atm) and the radius of the planet (R). The latitudes of the cylinder's edge (α) can then be derived from geometrical considerations as

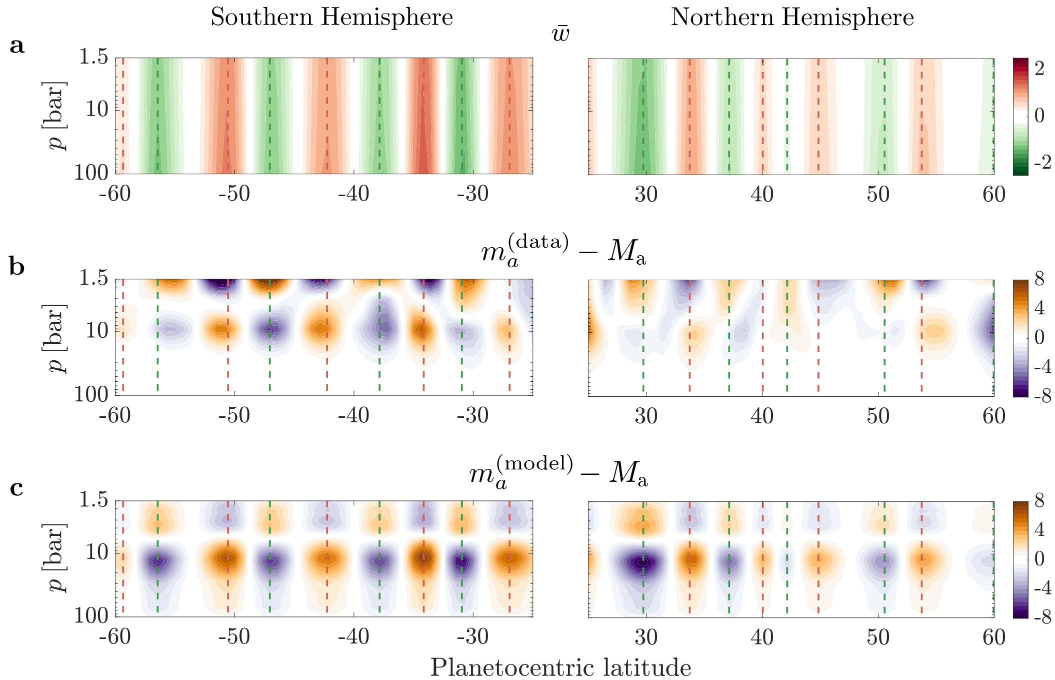

Figure S7: Model robustness analysis. An example for a model run without optimization. The optimized variables in this run are set manually according to physical considerations. The depth of the cells (a) is set to $1,500$ km such that the cells extend $3,000$ km in accordance with gravity measurements for the depth of the zonal jets [*Kaspi et al.*, 2018]. The relaxation constant G is set (without height dependence) from scaling argument by equating the relaxation term in equation 3 to the vertical advection term, leading to $G = \max(w)/a$. The value of σ is set to 0.5. (a) The normalized vertical velocity as a function of latitude and pressure. (b) The ammonia anomalies map that was reconstructed from Juno's MWR measurements. (c) The map of ammonia anomalies resultant from the degenerated model. It can be seen that the optimization procedure doesn't change the nature of the results which is robust. The structure of the anomalies stays largely the same both in this figure and in Fig. 4, and it stems mostly from the latitudinal structure of the wind and the vertical stratification of the ammonia, both being derived from observations.

$$\alpha = \arccos\left(1 - \frac{D_\mathrm{atm}}{R}\right). \tag{S14}$$

Gravity analysis reveals that Jupiter's atmosphere is approximately 3000 km deep [*Guillot et al.*, 2018; *Kaspi et al.*, 2018]. Substituting $D_\mathrm{atm} = 3000$ km and $R = R_\mathrm{J} = 70,000$ km in Eq. S14 gives $\alpha = \pm 16.8°$. This means that fluid columns parallel to the axis of rotation in the latitude range $-17° \leq \vartheta \leq 17°$, can theoretically extend uninterruptedly between the hemispheres.

S2.2 Theory for the leading balance in the Jovian equatorial region

Starting from the primitive equations[*Vallis*, 2017], the continuity and zonal momentum equations in spherical coordinates are

$$\frac{\partial \rho}{\partial t} + \rho\left(\frac{1}{R_\mathrm{J}\cos\vartheta}\frac{\partial u}{\partial \lambda} + \frac{1}{R_\mathrm{J}\cos\vartheta}\frac{\partial}{\partial \vartheta}\left(v\cos\vartheta\right) + \frac{\partial w}{\partial r}\right) + \frac{u}{R_\mathrm{J}\cos\vartheta}\frac{\partial \rho}{\partial \lambda} + \frac{v}{R_\mathrm{J}}\frac{\partial \rho}{\partial \vartheta} + w\frac{\partial \rho}{\partial r} = 0, \tag{S15}$$

and

$$\frac{\partial u}{\partial t} + \frac{u}{R_\mathrm{J}\cos\vartheta}\frac{\partial u}{\partial \lambda} + \frac{v}{R_\mathrm{J}}\frac{\partial u}{\partial \vartheta} + w\frac{\partial u}{\partial r} - 2\Omega\left(\sin\vartheta\, v - \cos\vartheta\, w\right) - \frac{uv}{R_\mathrm{J}}\tan\vartheta = -\frac{1}{R_\mathrm{J}\rho\cos\vartheta}\frac{\partial p}{\partial \lambda}, \tag{S16}$$

respectively, where λ is longitude. The mean density (ρ_m) is assumed to only change with r, and anomalies from it are assumed to be much smaller than the mean value. In addition, the meridional derivatives and the meridional velocity are assumed very small near the equator, relative to the other terms. This assumption is based on the symmetry around the equator. Assuming also a steady state, Eq. S15 and Eq. S16, evaluated on the equatorial plane ($\vartheta = 0°$), are then

$$\rho_m \left(\frac{1}{R_\mathrm{J}} \frac{\partial u}{\partial \lambda} + \frac{\partial w}{\partial r} \right) + w \frac{\partial \rho_m}{\partial r} = 0, \tag{S17}$$

and

$$\frac{u}{R_\mathrm{J}} \frac{\partial u}{\partial \lambda} + w \frac{\partial u}{\partial r} + 2\Omega w = -\frac{1}{R_\mathrm{J} \rho_m} \frac{\partial p}{\partial \lambda}. \tag{S18}$$

Eq. S18 can equivalently be represented as

$$\frac{1}{R_\mathrm{J}} \frac{\partial u^2}{\partial \lambda} + \frac{1}{\rho_m} \frac{\partial \left(w u \rho_m \right)}{\partial r} - \frac{u}{\rho_m} \left(\rho_m \frac{1}{R_\mathrm{J}} \frac{\partial u}{\partial \lambda} + \rho_m \frac{\partial w}{\partial r} + w \frac{\partial \rho_m}{\partial r} \right) + 2\Omega w = -\frac{1}{R_\mathrm{J} \rho_m} \frac{\partial p}{\partial \lambda}, \tag{S19}$$

where the third term vanishes according to Eq. S17. Next, the velocities are decomposed via Reynolds decomposition ($u = u' + \overline{u}, \quad w = w' + \overline{w}$), such that the zonal mean of Eq. S19 gives

$$-\frac{\partial \left(\overline{w'u'} \rho_m \right)}{\partial r} = \overline{w} \frac{\partial \left(\overline{u} \rho_m \right)}{\partial r} + 2\rho_m \Omega \overline{w} + \rho_m \overline{u} \frac{\partial \overline{w}}{\partial r}. \tag{S20}$$

This shows that the momentum originating from the eddy momentum flux convergence $\left(\frac{\partial \left(\overline{w'u'} \rho_m \right)}{\partial r} < 0 \right)$, which drives the equatorial superrotation [*Kaspi et al.*, 2009], is divided between the growing equatorial super-rotating jet $\left(\frac{\partial (\overline{u} \rho_m)}{\partial r} > 0, \overline{u} > 0 \right)$, the Coriolis force and another residual term. The growing equatorial jet has been shown in many numerical simulations of superrotation [*Heimpel et al.*, 2005; *Kaspi et al.*, 2009; *Gastine et al.*, 2014]. It is a good assumption that each of the terms on the right side is of smaller magnitude than the source term on the left side. Finally, rearranging Eq. S20 gives

$$\overline{w} = -\frac{1}{\underbrace{\frac{\partial \left(\overline{u} \rho_m \right)}{\partial r}}_{>0} + \underbrace{2\rho_m \Omega}_{>0}} \underbrace{\left(\frac{\partial \left(\overline{w'u'} \rho_m \right)}{\partial r} + \rho_m \overline{u} \frac{\partial \overline{w}}{\partial r} \right)}_{<0} > 0. \tag{S21}$$

To further simplify, Eq. S21 can be shown for the case of small Rossby number:

$$\overline{w} = -\frac{1}{2\rho_m \Omega} \frac{\partial \left(\overline{w'u'} \rho_m \right)}{\partial r} > 0. \tag{S22}$$

This implies that the mean upwelling ($\overline{w}$) correlates with eddy momentum flux convergence, and therefore with the equatorial superrotating jet at the equatorial region. Since the superrotating jet is supposed to be driven by angular momentum fluxes in the direction perpendicular to the rotation axis [*Heimpel et al.*, 2005; *Kaspi et al.*, 2009; *Schneider and Liu*, 2009], converging in the equatorial region, Eq. S22 would take the more general form

$$\overline{w_\perp} = -\frac{1}{2\rho_m \Omega} \partial_\perp \left(\overline{w'_\perp u'} \rho_m \right) > 0, \tag{S23}$$

where $w_\perp$ and $\partial_\perp$ are the velocity and the gradient in the direction perpendicular to the axis of rotation, i.e., $w_\perp = w \cos\vartheta + v \sin\vartheta$ and $\partial_\perp = (\cos\vartheta)\, \partial_r + \left(r^{-1} \sin\vartheta \right) \partial_\vartheta$.

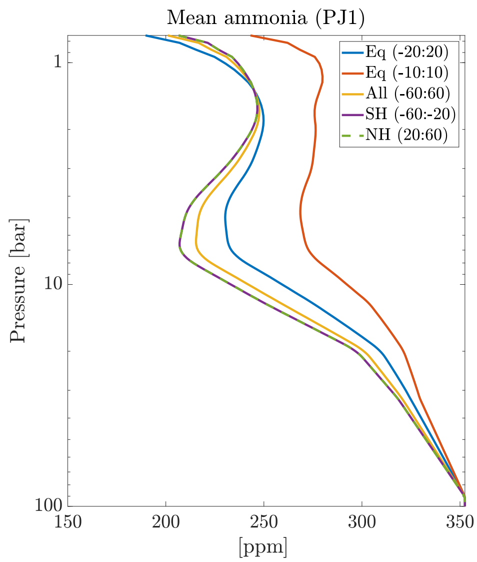

Figure S8: Meridional averaged ammonia values at different latitudinal regions. The lines are calculated according to the inferred ammonia map from PJ1 [*Li et al.*, 2017]. Each line is averaged at the latitudinal range described in the legend.

References

Bolton, S. J., et al., Jupiter's interior and deep atmosphere: The initial pole-to-pole passes with the Juno spacecraft, *Science*, *356*, 821–825, 2017.

Fletcher, L. N., et al., Jupiter's temperate belt/zone contrasts revealed at depth by Juno microwave observations, *Earth and Space Science Open Archive*, p. 35, doi:10.1002/essoar.10506297.1, 2021.

Galanti, E., and Y. Kaspi, Combined magnetic and gravity measurements probe the deep zonal flows of the gas giants, *Mon. Not. Roy. Astro. Soc.*, *501*(2), 2352–2362, 2021.

Galanti, E., et al., Constraints on the latitudinal profile of Jupiter's deep jets, *Geophys. Res. Lett.*, *48*(9), e2021GL092,912, 2021.

Gastine, T., J. Wicht, L. D. V. Duarte, M. Heimpel, and A. Becker, Explaining Jupiter's magnetic field and equatorial jet dynamics, *Geophys. Res. Lett.*, *41*, 5410–5419, 2014.

Guillot, T., et al., A suppression of differential rotation in Jupiter's deep interior, *Nature*, *555*, 227–230, 2018.

Heimpel, M., J. Aurnou, and J. Wicht, Simulation of equatorial and high-latitude jets on Jupiter in a deep convection model, *Nature*, *438*, 193–196, 2005.

Janssen, M. A., et al., MWR: Microwave Radiometer for the Juno Mission to Jupiter, *Space Sci. Rev.*, *213*(1-4), 139–185, doi:10.1007/s11214-017-0349-5, 2017.

Kaspi, Y., G. R. Flierl, and A. P. Showman, The deep wind structure of the giant planets: Results from an anelastic general circulation model, *Icarus*, *202*, 525–542, 2009.

Kaspi, Y., E. Galanti, A. P. Showman, D. J. Stevenson, T. Guillot, L. Iess, and S. J. Bolton, Comparison of the deep atmospheric dynamics of Jupiter and Saturn in light of the Juno and Cassini gravity measurements, *Space Sci. Rev.*, *216*(5), 1–27, 2020.

Kaspi, Y., et al., Jupiter's atmospheric jet-streams extend thousands of kilometres deep, *Nature*, *555*, 223–226, 2018.

Lachmy, O., and Y. Kaspi, The role of diabatic heating in Ferrel cell dynamics, *Geophys. Res. Lett.*, *47*(23), e2020GL090,619, 2020.

Lee, S., and Y. Kaspi, Towards an understanding of the structure of Jupiter's atmosphere using the ammonia distribution and the Transformed Eulerian Mean theory, *J. Atmos. Sci.*, *78*(7), 2047–2056, 2021.

Li, C., et al., The distribution of ammonia on Jupiter from a preliminary inversion of Juno microwave radiometer data, *Geophys. Res. Lett.*, *44*(11), 5317–5325, 2017.

Liu, J., and T. Schneider, Mechanisms of jet formation on the giant planets, *J. Atmos. Sci.*, *67*, 3652–3672, 2010.

Liu, J., P. M. Goldreich, and D. J. Stevenson, Constraints on deep-seated zonal winds inside Jupiter and Saturn, *Icarus*, *196*, 653–664, 2008.

Oyafuso, F., et al., Angular dependence and spatial distribution of Jupiter's centimeter-wave thermal emission from Juno's microwave radiometer, *Earth Planet. Sci. Lett.*, *7*(11), e2020EA001,254, doi: https://doi.org/10.1029/2020EA001254, 2020.

Schneider, T., and J. Liu, Formation of jets and equatorial superrotation on Jupiter, *J. Atmos. Sci.*, *66*, 579–601, 2009.

Tollefson, J., et al., Changes in Jupiter's zonal wind profile preceding and during the Juno mission, *Icarus*, *296*, 163–178, 2017.

Vallis, G. K., *Atmospheric and Oceanic Fluid Dynamics*, second ed., pp. 770. Cambridge University Press., 2017.